

DriveSplat: Decoupled Driving Scene Reconstruction with Geometry-enhanced Partitioned Neural Gaussians

Cong Wang^{1,2*}, Xianda Guo^{3*†}, Wenbo Xu⁴, Wei Tian⁵, Ruiqi Song^{1,4}, Chenming Zhang⁶, Lingxi Li⁷, Long Chen^{1,4,6‡}

¹the State Key Laboratory of Multimodal Artificial Intelligence Systems, Institute of Automation, Chinese Academy of Sciences ²School of Artificial Intelligence, University of Chinese Academy of Sciences

³School of Computer Science, Wuhan University ⁴Waytous ⁵School of Automotive Studies, Tongji University

⁶Institute of Artificial Intelligence and Robotics, Xi'an Jiaotong University ⁷Purdue University

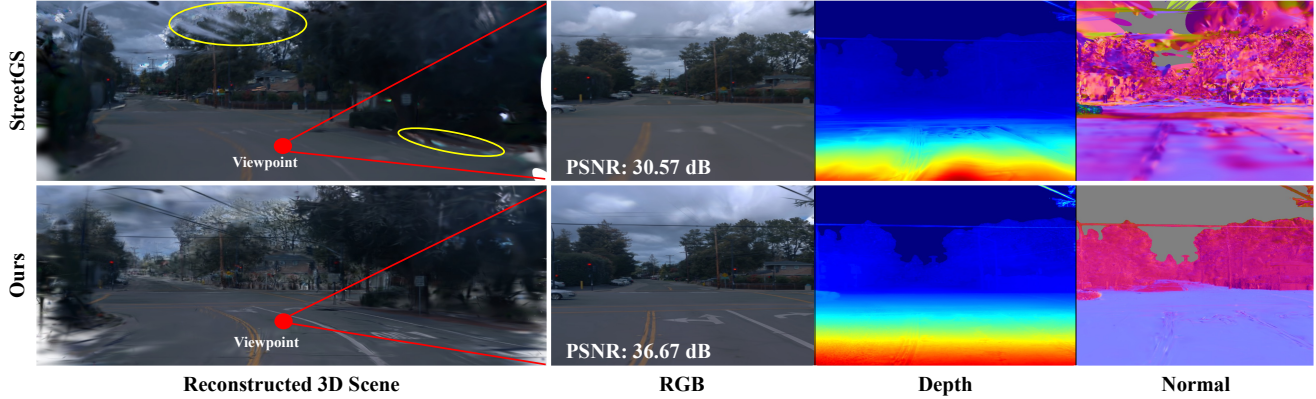


Figure 1: **Comparison with StreetGS.** StreetGS generates an excessive number of redundant Gaussians (yellow circles) in the reconstructed 3D scene. The right panel presents the rendered image, depth and normal map from a novel view (red dots).

Abstract

In the realm of driving scenarios, the presence of rapidly moving vehicles, pedestrians in motion, and large-scale static backgrounds poses significant challenges for 3D scene reconstruction. Recent methods based on 3D Gaussian Splatting address the motion blur problem by decoupling dynamic and static components within the scene. However, these decoupling strategies overlook background optimization with adequate geometry relationships and rely solely on fitting each training view by adding Gaussians. Therefore, these models exhibit limited robustness in rendering novel views and lack an accurate geometric representation. To address the above issues, we introduce DriveSplat, a high-quality reconstruction method for driving scenarios based on neural Gaussian representations with dynamic-static decoupling. To better accommodate the predominantly linear motion patterns of driving viewpoints, a region-wise voxel initialization scheme is employed, which partitions the scene into near, middle, and far regions to enhance close-range detail representation. Deformable neural Gaussians are introduced to model non-rigid dynamic actors, whose parameters are temporally adjusted by a learnable deformation network. The entire framework is further supervised by depth and normal priors from pre-trained models, improving the accuracy of geometric structures. Our method has been rigorously evaluated on the Waymo and KITTI datasets, demonstrating state-of-the-art performance in novel-view synthesis for driving scenarios. Project page: <https://physwm.github.io/drivesplat>.

Introduction

The 3D simulation of autonomous driving scenarios can greatly facilitate closed-loop testing of autonomous driving functions. Furthermore, it allows for the flexible construction of complex traffic environments, which can be used to train perception and decision-making models. Compared to traditional methods such as oblique photography or manually constructed simulation environments, 3D reconstruction and novel view synthesis (NVS) techniques can reconstruct 3D scenes from 2D image inputs, offering advantages in both convenience and realism (Yang et al. 2023).

In the related domain, the pioneering NeRF method (Mildenhall et al. 2021; Barron et al. 2021) introduces implicit scene reconstruction through ray sampling, offering a novel technical paradigm for the field of 3D reconstruction. The 3D Gaussian Splatting (3D-GS)(Kerbl et al. 2023) further improves the reconstruction efficiency by explicitly representing the scene with Gaussian ellipsoids, which effectively enhances the rendering speed. These methods (Mildenhall et al. 2021; Kerbl et al. 2023) have achieved promising results in object-centric scenes and small indoor environments. Subsequent works (Yu et al. 2024; Lu et al. 2024; Ren et al. 2025; Zhang et al. 2024) have further improved the robustness of reconstruction to viewpoint variations and enhanced scalability to large-scale scenes. Among them, neural Gaussian representations (Lu et al. 2024; Ren et al. 2025) have emerged as an effective

*Equal contribution; †Project leader; ‡Corresponding author.

approach that balances novel view synthesis quality with reconstruction efficiency. Nevertheless, the 3D reconstruction in driving scenarios presents greater challenges (Kerbl et al. 2024; Li et al. 2024; Chen et al. 2023; Huang et al. 2024b; Yan et al. 2024; Zhou et al. 2024) due to the presence of fast-moving vehicles, which are difficult to capture accurately and thus introduce motion blur into the scene. To address these challenges, StreetGS (Yan et al. 2024) and DrivingGaussian (Zhou et al. 2024) utilize a dynamic-static decoupling strategy, which effectively separates the reconstruction of dynamic foreground actors from static backgrounds. Subsequent research start to optimize non-rigid dynamic actors (Chen et al. 2025), refine trajectories of dynamic entities (Ma et al. 2025), and seek for dynamic decoupling method utilizing flow or semantic (Sun et al. 2025; Xu et al. 2025). However, these methods still rely on the original 3D-GS representation for background reconstruction, which lacks robustness in challenging novel view synthesis and does not adequately address geometric accuracy.

Addressing the above crucial gap, our work aims to provide a view-robust and geometry-accurate reconstruction framework for dynamic driving scenarios. In contrast to training viewpoints that steadily improve rendering through supervision, novel viewpoints increase variability, challenging consistent scene reconstruction. The 3D-GS series models (Kerbl et al. 2023; Yan et al. 2024; Zhou et al. 2024; Huang et al. 2024b) enhance rendering performance at training viewpoints by incrementally adding Gaussian ellipsoids; however, this can lead to redundant Gaussian ellipsoids that result in blurriness and noise when observed from alternative perspectives. Previous reconstruction methods for driving scenarios have relied on LiDAR for depth supervision, yet LiDAR fails to provide pixel-wise depth ground truth, particularly lacking effective supervision for tall buildings and distant objects. Additionally, these methods have not adequately addressed the optimization of surface quality in the reconstruction model, resulting in poor normal map outcomes, as illustrated in Fig. 1.

To address these mutually reinforced challenges, we propose DriveSplat, a viewpoint-robust reconstruction framework based on neural Gaussian representations with dynamic-static decoupling. Anchored by fused point clouds from Structure-from-Motion (SfM) and LiDAR, we separate dynamic points from the static background and use them to independently initialize foreground actors and background representation. An octree-based partitioned voxel structure is then constructed over these spatial anchors, with multi-level voxel representations corresponding to different levels of detail (LOD). Driving scenarios typically exhibit denser point distributions in the near and middle ranges. To better capture fine-grained details in these regions, we estimate the scene’s principal axis and segment it into near, middle, and far regions by using a clustering algorithm. Voxel sizes in the near and middle zones are refined to better fit the dense point distributions. For dynamic actors in the scene, we use bounding box information to transform each reconstructed instance from local to global coordinates. For non-rigid dynamic actors such as pedestrians and cyclists, we

additionally design a deformation network that models the temporal evolution of neural Gaussians by adjusting their attributes (e.g., position, rotation, scale) over time. To further improve geometric quality, we supervise the reconstruction using dense depth and surface normal maps predicted by pre-trained monocular models, ensuring accurate geometric consistency in rendering. In conclusion, our main contributions are summarized as follows:

- We introduce neural Gaussian representation into driving scene reconstruction and propose a near-mid-far partitioned background optimization module that enhances the representation of close-range details, significantly improving performance in novel view synthesis tasks.
- We adopt a dynamic-static decoupled scene representation strategy, unifying the use of neural Gaussians to model both static backgrounds and dynamic actors. Additionally, we introduce deformable neural Gaussians to reconstruct non-rigid actors.
- We investigate the role of depth and normal priors in improving both the rendering quality and geometric accuracy. Our method achieves state-of-the-art performance in NVS tasks on both the Waymo and KITTI datasets.

Related Works

Large-scale Scene Reconstruction

The naive NeRF (Mildenhall et al. 2021) struggles with large-scale scenes due to blurry close-ups and jagged distant edges. Improvements include Mip-NeRF (Barron et al. 2021) with multi-scale IPE, NeRF-W (Martin-Brualla et al. 2021) for lighting variations, and Block-NeRF (Tancik et al. 2022), which trains local blocks separately. Recently, 3D-GS-based methods (Kerbl et al. 2023; Yu et al. 2024; Liu et al. 2025a) have achieved remarkable breakthroughs in both reconstruction speed and quality. The initial Gaussian Splatting (Kerbl et al. 2023) is specifically designed for scenes with an object-centred view, and subsequent efforts have extended it to large-scale scenes. Neural Gaussian (Lu et al. 2024; Ren et al. 2025) incorporates the advantage of Gaussian Splatting and neural fields, and achieves real-time rendering with robust viewpoint invariance. Hierarchical-GS (Kerbl et al. 2024) introduces a hierarchical structure for driving scenes to optimize the effect of real-time reconstruction and combines the blocking strategy to select different levels. For the urban scene reconstruction, some methods (Lin et al. 2024; Liu et al. 2025b; Ren et al. 2025) propose to divide point clouds into cells, and introduce the Level-of-Details to optimize reconstruction efficiency and detail performance. Above methods neglect dynamic object optimization, while our approach improves reconstruction by decoupling dynamic and static components.

Dynamic Scene Reconstruction

Traditional reconstruction methods (Mildenhall et al. 2021; Kerbl et al. 2023; Yu et al. 2024) primarily focus on static scenes and are unable to represent dynamic scenes or objects with temporal variations, leading to issues such as motion blur. The NeRF (Mildenhall et al. 2021) leverages MLPs

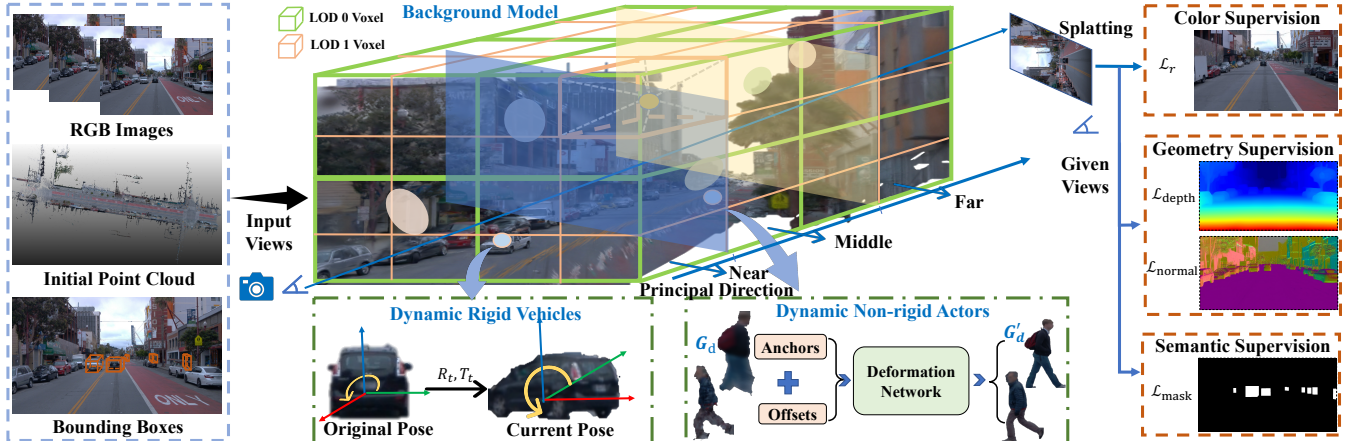


Figure 2: **Overall pipeline of DriveSplat.** A dynamic-static decoupling paradigm is adopted, where neural Gaussian representations with partitioned voxel structures are applied for background reconstruction, while a deformation field network models the temporal dynamics of each non-rigid actor. Depth maps and normal priors are incorporated to enhance geometric accuracy.

for implicit modeling of static environments. This concept has been extended to animate scenarios through the integration of deformation fields (Guo et al. 2023; Park et al. 2021; Pumarola et al. 2021). Alternatively, certain strategies (Park et al. 2023) conceptualize animate scenes as 4D radiance landscapes, albeit at the cost of significant computational resources attributed to ray-point sampling and volumetric rendering. To mitigate these issues, acceleration techniques (Li et al. 2023; Lin et al. 2022) have been devised for the depiction of dynamic environments. Some methods include the use of geometry priors (Lombardi et al. 2021), the projection of MLP-derived mappings (Peng et al. 2023), or the implementation of grid/plane-oriented architectures (Cao and Johnson 2023) to elevate both the speed and efficacy. Several works adapt 3D Gaussians for dynamic scenes (Sun et al. 2025; Xu et al. 2025; Ma et al. 2025). Luiten et al. (Luiten et al. 2023) train frame-by-frame for multi-view scenes, while Yang et al. (Yang et al. 2024b) use a deformation field to represent the temporal changes of objects. 4D-GS (Wu et al. 2024) propose to use multi-resolution hex-planes (Cao and Johnson 2023) to encode deformed motion. We learn from the above 4D reconstruction methods and adopt a deformation field to model the temporal evolution of neural Gaussians for non-rigid actors.

Geometry Optimization in 3D Reconstruction

Depth and normal supervision enhance scene reconstruction by improving geometric accuracy and surface orientation, enabling high-fidelity capture of complex scenes (Zhu et al. 2023; Jiang et al. 2023). Several methods (Wei et al. 2021; Liu et al. 2025a) propose to integrate depth priors to guide the reconstruction process. The following works (Roessle et al. 2022; Wang et al. 2023) propose embedding depth supervision into the NeRF framework to boost training efficiency and reduce multi-view input dependency. MVS-Gaussian (Liu et al. 2025a) combines MVS with Gaussian Splatting to improve reconstruction in sparse-view settings. DN-Splatter (Turkulainen et al. 2024) presents an innovative approach by utilizing depth-normal fusion to enhance point cloud precision in complex environments, while 2D-

GS (Huang et al. 2024a) leverages 2D depth maps to refine the Gaussian Splatting technique for more efficient reconstruction in real-time applications. In driving scenarios, GaussianPro (Cheng et al. 2024) introduces a progressive propagation strategy that focuses on optimizing geometric properties. And Desire-GS (Peng et al. 2025) proposes the combination of geometric priors for enhanced supervision, but faces problems of very slow training speeds. Drawing on the above methods, we utilize depth and normal priors to guide neural Gaussian reconstruction, enhancing geometric quality while maintaining reconstruction efficiency.

Methology

As shown in Fig. 2, the inputs to DriveSplat include RGB images, an initialized 3D point cloud, and bounding boxes of dynamic actors provided by the dataset. Depth and normal priors predicted by pre-trained models are utilized during the supervised optimization stage.

Neural Gaussians Initialization in Street Scenarios

Point Cloud Initialization. DriveSplat supports multiple types of point cloud initialization, including SfM, LiDAR, and dense DUST3R (Wang et al. 2024) input. Our model separates dynamic actors by leveraging tracked bounding boxes to estimate their pose parameters ($\mathbf{q}_{\text{obj}}, \mathbf{t}_{\text{obj}}$), which are used to compute a transformation matrix \mathbf{T}_{obj} . When LiDAR data is available, each frame's point cloud $\mathbf{P}_{\text{frame}}$ is then transformed into the actor's local coordinate system for consistent modeling. Within the local coordinate system, an axis-aligned bounding box \mathcal{B} is constructed to identify and filter the points \mathbf{P}_{obj} enclosed within it. This process is applied to all tracked actors, generating dynamic actor point cloud masks \mathbf{M}_{obj} .

$$\mathbf{P}_{\text{obj}} = \bigcup_i \left\{ \mathbf{P}_{\text{frame}}^{(i)} \mathbf{T}_{\text{obj}}^{-1} \mid \mathbf{M}_{\text{obj}}^{(i)} = 1 \right\}. \quad (1)$$

The remaining unmasked points are classified as static points, defined as:

$$\mathbf{P}_{\text{s}} = \{ \mathbf{p} \mid \mathbf{p} \in \mathbf{P}_{\text{frame}}, \mathbf{M}_{\text{obj}}(\mathbf{p}) = 0 \}. \quad (2)$$

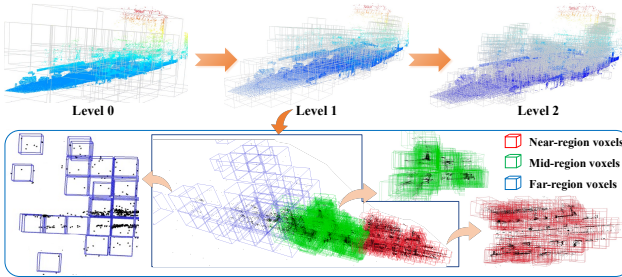


Figure 3: **Visualization of voxel representation at different levels.** As the level increases, the voxel resolution gradually improves. The corresponding partitioned neural Gaussians are shown in the bottom row.

In the absence of LiDAR data, our method initializes the point cloud of dynamic actors by randomly initializing points within the bounding boxes in the relative coordinate system. For static background points, when LiDAR is not used, we directly use COLMAP’s point cloud for initialization, as it contains only static points.

Static Background Representation. Subsequently, we initialize the background representation model using the octree structure and introduce an optimization method for the driving scenario. Following Octree-GS (Ren et al. 2025), we calculate the octree layer number O determined by the predicted depth range $(\hat{d}_{\min}, \hat{d}_{\max})$. The octree structure is constructed across multiple LOD, where all occupied voxel centers $\mathbf{V} \in \mathbf{R}^{M \times 3}$ are computed by quantizing the point cloud \mathbf{P} at different levels. The base voxel size γ is calculated by dividing the initial voxel size ϵ by powers of two, i.e., $\gamma = \epsilon/2^l, l = 0, 1, \dots, O-1$. The base voxel size decreases with increasing levels, as illustrated in Fig. 3. Anchor points μ_a are chosen as voxel centers, ensuring $\mu_a \in \mathbf{V}$.

For large-scale point clouds with significant depth variation, directly applying octree voxelization often leads to oversized voxels, as distant sparse background points dominate the global voxel size. Since close-range points are typically denser and contribute more to image-space projection, enhancing their reconstruction is crucial. A distance-aware hierarchical scheme is introduced for point cloud partitioning, forming the basis of the background partitioned optimization (BPO) module. PCA (Mackiewicz and Ratajczak 1993) is used to estimate the principal axis, along which near and far ends are determined with respect to the initial camera pose. The direction of the principal axis is the principal direction. All initial points are projected along the principal axis. A Gaussian Mixture Model (GMM) is applied along this axis to obtain partitioning thresholds h_1 and h_2 , dividing the projected points into near, middle, and far regions. To account for the variations in point cloud sparsity across different regions, we have developed an adaptive voxel construction strategy based on partitioning along the principal axis direction. Then we calculate the voxel size $v(\mu_a)$ for a position μ_a as follows:

$$v(\mu_a) = \begin{cases} \frac{\gamma}{\phi_1}, & \text{if } \mu_a \in \text{near region} \\ \frac{\gamma}{\phi_2 + \bar{\rho}}, & \text{if } \mu_a \in \text{middle region} \\ \frac{\gamma}{1 + \rho_{\min}}, & \text{if } \mu_a \in \text{far region} \end{cases} \quad (3)$$

where γ denotes the base voxel size, $\bar{\rho}$ and ρ_{\min} represent the mean and minimum normalized inverse density among the projected points. The normalized inverse density is computed by discretizing points along the principal axis into bins and calculating the reciprocal of point counts in each bin. These values are then normalized by their maximum. Parameters ϕ_1 and ϕ_2 are predefined scaling factors satisfying $\phi_1 > \phi_2 > 1$, controlling the degree of voxel refinement in different regions.

The neural Gaussian is then computed using an anchor point location μ_a , a scaling factor f_a , and corresponding learnable offsets \mathcal{X}_i (Lu et al. 2024) as follows:

$$\{\mu_0, \dots, \mu_{O-1}\} = \mu_a + \{\mathcal{X}_0, \dots, \mathcal{X}_{O-1}\} \cdot f_a. \quad (4)$$

Finally, we established neural Gaussian representations in three regions, as illustrated in Fig. 3.

Dynamic Actors Representation

For a scene containing several moving foreground dynamic actors, each actor is described by a set of adjustable tracked poses and a point cloud. At initialization, the actor’s Gaussians use the point cloud \mathbf{P}_{obj} as anchors, and a semantic label is assigned to differentiate it from the background and specify whether it is rigid.

Dynamic Actor Pose Transformation. The structure of Gaussians for both actors and the background is similar, with the opacity α_o and scale matrix \mathbf{S}_o defined identically. The position μ_o and rotation \mathbf{R}_o for an actor are defined within the actor’s local coordinate system. To align with the background, these variables must be transformed into the world coordinate system, which requires applying the actor’s tracked poses. Specifically, these tracked poses are represented by a set of rotation matrices $\{\mathbf{R}_t\}_{t=1}^{N_t}$ and translation vectors $\{\mathbf{T}_t\}_{t=1}^{N_t}$, where N_t denotes the total number of frames. This transformation is expressed as

$$\begin{aligned} \mu &= \mathbf{R}_t \mu_o + \mathbf{T}_t, \\ \mathbf{R} &= \mathbf{R}_o \mathbf{R}_t^T, \end{aligned} \quad (5)$$

where μ and \mathbf{R} denote the position and rotation of the dynamic actor’s Gaussians \mathbf{G}_d within the world coordinate system.

Non-rigid Actor Representation. For non-rigid dynamic actors, we first extract the anchor and offset points from all associated neural Gaussians. These are combined to form a unified representation:

$$\mathcal{P} = \{\mu_i + \mathcal{X}_j \mid i = 1, \dots, N, j = 1, \dots, O\}, \quad (6)$$

where μ_i denotes the anchor point of the i -th Gaussian, and \mathcal{X}_j is its corresponding positional offset at level j . Building on previous 4D reconstruction methods (Wu et al. 2024; Yang et al. 2024b), we utilize a deformation network to learn the deformed position, scale, and rotation of \mathbf{G}_d at a specific time t , and obtain the deformed dynamic Gaussians \mathbf{G}'_d .

Finally, we get the combined neural Gaussians \mathbf{G} by concatenating the static Gaussians \mathbf{G}_s , dynamic Gaussians \mathbf{G}_d , and deformed Gaussians \mathbf{G}'_d . The rendered image I , depth map D and normal map N are obtained via Splatting:

$$\{I, D, N\} = \mathcal{S}(M, G), \quad (7)$$

where M denotes the camera view matrix for current frame.



Figure 4: Qualitative novel-view synthesis results on the Waymo dataset. Patches that highlight the visual differences are emphasized with red boxes and enlarged for clearer visibility. The rendering image resolution is 1066×1600 .

Geometry Enhanced Optimization

Geometry Prior Estimation. We utilize depth and normal priors to guide the geometry optimization process. To obtain per-pixel referenceable depth values, monocular depth estimation can be employed to predict either absolute depth D_m or relative depth D_r . We use the DepthAnything-V2 (Yang et al. 2024a) model for relative depth estimation and the ZoeDepth (Bhat et al. 2023) model for absolute depth estimation. To obtain reliable surface normal priors, we leverage a pre-trained normal estimation model (Eftekhar et al. 2021) to generate normal maps N_m . These estimated normals provide crucial geometric constraints, contributing to improved surface quality of the reconstructed driving scenario.

Loss Functions. To achieve a high-quality rendering, we define a comprehensive loss function as:

$$\mathcal{L} = \mathcal{L}_r + \lambda_d \mathcal{L}_{\text{depth}} + \lambda_n \mathcal{L}_{\text{normal}} + \lambda_m \mathcal{L}_{\text{mask}}, \quad (8)$$

where \mathcal{L}_r , $\mathcal{L}_{\text{depth}}$, $\mathcal{L}_{\text{normal}}$, $\mathcal{L}_{\text{mask}}$ represent the rendered color loss, depth loss, normal loss, and dynamic actor mask loss, respectively. Here, λ_d , λ_n , and λ_m are hyperparameters that control the weights of each loss term during optimization.

The rendering color loss \mathcal{L}_r incorporates an L1 loss $\mathcal{L}_{\text{L1}}(I, I_{\text{gt}})$ and a structural similarity index loss $\mathcal{L}_{\text{SSIM}}(I, I_{\text{gt}})$, defined as:

$$\mathcal{L}_r = \mathcal{L}_{\text{L1}}(I, I_{\text{gt}}) + \lambda \mathcal{L}_{\text{SSIM}}(I, I_{\text{gt}}), \quad (9)$$

where λ balances the contribution of the L1 loss and SSIM loss to achieve high-quality rendering results.

To further enhance geometric accuracy, we include the depth loss $\mathcal{L}_{\text{depth}}$, to enforce consistency between our estimated depth map D and the predicted relative depth map D_r . This loss is scaled by weight λ_d and computed using correlation loss:

$$\mathcal{L}_{\text{depth}} = \left\| \frac{\text{Cov}(D, D_r)}{\sqrt{\text{Var}(D)\text{Var}(D_r)}} \right\|_1, \quad (10)$$

where $\text{Cov}(\cdot)$ and $\text{Var}(\cdot)$ denote the covariance and variance, respectively. Our method also supports supervision using absolute depth D_m , where the L1 loss is used rather than the correlation loss.

To ensure that the predicted surface normals align with the real surface normal distribution, we incorporate the normal loss $\mathcal{L}_{\text{normal}}$. The loss includes L1 loss $\mathcal{L}_{n_{\text{L1}}}$ for error between our estimated normal N and predicted reference normal N_m , and cosine similarity loss $\mathcal{L}_{n_{\text{cos}}}$ for normal direction alignment. The total normal loss is:

$$\mathcal{L}_{\text{normal}} = \mathcal{L}_{n_{\text{L1}}}(N, N_m) + \mathcal{L}_{n_{\text{cos}}}(N, N_m). \quad (11)$$

In addition, the mask loss $\mathcal{L}_{\text{mask}}$ employs cross-entropy to compare predicted and ground-truth masks, helping to improve rendering quality of dynamic actors.

Experiments

Datasets

Waymo (Sun et al. 2020) offers a diverse range of sensor data from both urban and suburban settings. We chose 8 sequences recorded under various conditions, including different weather (e.g., foggy and sunny) and traffic scenarios (e.g., city slow roads and highways). Additionally, two sequences utilized in OmniRe (Chen et al. 2025) were selected for an ablation study to verify non-rigid actor reconstruction performance.

KITTI (Geiger, Lenz, and Urtasun 2012) includes numerous scenes with significant lighting variations, ranging from high-exposure areas to shadowed regions, creating substantial challenges for reconstruction. Therefore, evaluating the reconstruction performance on sequences from the KITTI dataset provides a robustness test of the model’s resilience to varying environmental conditions. We select 3 sequences containing both dynamic non-rigid actors and challenging backgrounds to perform comparative experiments.

Implementation Details

We assess our method’s performance in training-view reconstruction and novel-view synthesis by sampling every fourth frame from the original sequence, excluding them from model training. Training a scene of 30K iterations takes 68 minutes on a single NVIDIA L20 GPU, far more efficient than Desire-GS’s over 180 minutes (see Appendix Table 2).

Model	Type	D_{opt}	N_{opt}	Scene Reconstruction			Novel View Synthesis		
				PSNR↑	SSIM↑	LPIPS↓	PSNR↑	SSIM↑	LPIPS↓
3D-GS (Kerbl et al. 2023)	Static	✗	✗	33.27	0.935	0.102	30.93	0.926	0.108
GaussianPro (Cheng et al. 2024)	Static	✓	✓	32.79	0.928	0.113	31.28	0.915	0.121
Octree-GS (Ren et al. 2025)	Static	✗	✗	33.63	0.936	0.103	32.13	<u>0.927</u>	<u>0.107</u>
4D-GS (Wu et al. 2024)	Dynamic	✗	✗	31.01	0.890	0.205	28.16	0.870	0.219
Deform-GS (Yang et al. 2024b)	Dynamic	✗	✗	32.66	0.912	0.158	30.19	0.896	0.167
S3Gaussian (Huang et al. 2024b)	Dynamic	✓	✗	33.44	0.927	0.118	31.62	0.917	0.124
PVG (Chen et al. 2023)	Dynamic	✓	✗	34.89	0.941	<u>0.093</u>	32.45	0.917	0.112
StreetGS (Yan et al. 2024)	Dynamic	✗	✗	35.66	0.936	0.109	30.87	0.882	0.139
OmniRe (Chen et al. 2025)	Dynamic	✓	✗	34.95	0.943	0.114	31.79	0.905	0.125
Desire-GS (Peng et al. 2025)	Dynamic	✓	✓	34.55	0.926	0.108	32.56	0.919	0.119
AD-GS (Xu et al. 2025)	Dynamic	✓	✗	<u>35.76</u>	0.939	0.104	<u>33.46</u>	0.925	0.114
Ours	Dynamic	✓	✓	36.08	<u>0.943</u>	0.079	34.41	0.928	0.087

Table 1: **Quantitative comparison results on Waymo dataset.** D_{opt} and N_{opt} denote depth and normal optimization, respectively. The image resolution is 1066×1600 . LPIPS uniformly adopts the AlexNet. **Bold:** Best. Underline: Second Best.



Figure 5: **Qualitative NVS comparison results on the KITTI dataset.** The rendering image resolution is 370×1226 .

Benchmark Evaluation

Results on Waymo. We evaluate our approach against established methods, including both static methods and dynamic methods, and use both reconstruction and novel view synthesis metrics on the Waymo dataset (Table 1). Our method surpasses all baselines in both PSNR and LPIPS reconstruction metrics, showcasing high precision. While StreetGS (Yan et al. 2024) and OmniRe (Chen et al. 2025) perform well in reconstruction metrics, they struggle with novel view synthesis, highlighting their limitations in handling viewpoint transitions. In contrast, DriveSplat excels in novel view synthesis tasks, outperforming all baselines across three evaluation metrics. Visual analysis (Fig. 4) highlights DriveSplat’s superior artifact-free rendering of vehicles, enhanced clarity of challenging static background details, and accurate depiction of dynamic vehicles. We further present novel view synthesis comparisons under a more challenging setting, with the ego-car trajectory shifted 1.0 meters left and 1.0 meters upward, as illustrated in Fig. 6.

Results on KITTI. The performance of DriveSplat is also evaluated on the KITTI dataset. As detailed in Table 2, DriveSplat outperforms baselines in both reconstruction and novel view synthesis tasks. Fig. 5 highlights rendering results, where DriveSplat demonstrates superior background clarity and accurate rendering of dynamic vehicles. Compared to OmniRe (Chen et al. 2025), our method demon-

Model	Scene Reconstruction			Novel View Synthesis		
	PSNR↑	SSIM↑	LPIPS↓	PSNR↑	SSIM↑	LPIPS↓
3D-GS	24.43	0.817	0.162	20.10	0.678	0.224
Octree-GS	23.51	0.738	0.288	21.90	0.679	0.300
GaussianPro	23.51	0.788	0.181	18.47	0.607	0.277
4D-GS	24.43	0.735	0.280	18.12	0.562	0.338
Deform-GS	27.64	0.810	<u>0.113</u>	<u>22.01</u>	<u>0.727</u>	<u>0.156</u>
OmniRe	28.68	<u>0.874</u>	0.115	20.86	0.592	0.187
Ours	<u>28.59</u>	0.895	0.100	24.53	0.767	0.142

Table 2: **Quantitative results on KITTI dataset.** The rendering image resolution is 370×1226 .

strates improved performance in novel view synthesis, particularly in preserving background details, as illustrated in the second row of Fig. 5.

Ablation Study

Ablation Study on Initialization Module. We evaluate the impact of different initialization methods, as shown in Table 3. LiDAR delivers the most precise point clouds but lacks coverage for tall buildings and distant areas. Although SfM provides sparser points, it offers broader scene coverage and thus slightly outperforms LiDAR alone. DUS3R yields the densest point clouds, but due to misalignment



Figure 6: Challenging novel-view synthesis comparison.

Initialization	PSNR↑	SSIM↑	LPIPS↓	Abs Rel↓
Random	29.93	0.901	0.123	0.253
SfM	33.30	0.913	0.126	0.236
LiDAR	32.01	0.906	0.124	0.157
DUS3R	31.81	0.894	0.115	0.202
SfM+LiDAR *	34.41	0.928	0.087	0.172

Table 3: Ablation study of the point cloud initialization module. Results are from novel view synthesis on the Waymo dataset. The asterisk (*) indicates our final choice.

in scale and position with real-world coordinates, even after transformation, its performance is suboptimal. Consequently, we selected the SfM+LiDAR combination for initialization, which produced the best rendering results.

Despite the point cloud initialization verification, we also conduct an ablation study on the partitioned background optimization module. We compare the performance of our method both with and without the background optimization module, as shown in Table 4. The results show that the BPO module can improve the performance of the method, which is also suitable for the Octree-GS (Ren et al. 2025).

Ablation Study on Geometry Optimization. We conducted depth and normal rendering experiments using GaussianPro (Cheng et al. 2024) as a baseline due to its high geometric accuracy in driving scenarios. For depth evaluation, we compare our method using depth priors (including metric depth D_m and relative depth D_r) and without, as shown in Table 5. We use 3 standard metrics: Absolute Relative Error (Abs Rel), Mean Absolute Error (MAE), and the accuracy under threshold ($\delta < 1.25$), together with PSNR to assess the quality of rendered images. Our method surpasses the baseline across all metrics. While metric depth D_m yields the most accurate depth, it reduces rendering quality. Conversely, relative depth D_r enhances rendering but lessens depth accuracy. This trade-off is due to the limited accuracy of absolute depth data, leading us to prefer relative depth for better overall quality. For normal evaluation, we assess our method both with and without normal priors, as presented in Table 5, using the estimated normals, N_m as referenced GT. We select 3 normal evaluation metrics: MAE, Root Mean Square Error (RMSE) and cosine similarity (cos sim). The result shows that our method outperforms the baseline in all metrics and proves the effectiveness of the normal priors.

Ablation Study on Dynamic Optimization Module. We additionally select two Waymo sequences that contain many

Model	PSNR↑	SSIM↑	LPIPS↓
Octree-GS (w/o BPO)	32.13	0.927	0.107
Octree-GS (w/ BPO)	32.69	0.929	0.098
Ours (w/o BPO)	33.82	0.926	0.093
Ours (w/ BPO) *	34.41	0.928	0.087

Table 4: Ablation study on background partitioned optimization module. BPO refers to the background partitioned optimization module.

Depth Model	AbsRel↓	MAE↓	$\delta 1.25 \uparrow$	PSNR↑
GaussianPro	0.513	9.06	59.11	31.28
Ours (w/o $\mathcal{L}_{\text{depth}}$)	0.234	5.19	68.91	33.44
Ours (D_m)	0.121	3.43	85.67	33.23
Ours (D_r) *	0.172	3.92	78.69	34.41

Normal Model	MAE↓	RMSE↓	cos sim↑	PSNR↑
GaussianPro	1.66	2.19	-0.023	31.28
Ours (w/o $\mathcal{L}_{\text{normal}}$)	1.05	1.72	0.331	34.28
Ours (w/ $\mathcal{L}_{\text{normal}}$) *	0.78	1.43	0.504	34.41

Table 5: Quantitative ablation study results of depth and normal optimization module.

pedestrians in front views to evaluate our non-rigid actor reconstruction performance. Decoupling dynamic and static elements in the scene effectively improves rendering quality for moving actors. Adding individual dynamic object representation can improve the rendering quality of moving vehicles, but it still suffers from motion blur for non-rigid actors. After adding the deformable module, the rendering quality of non-rigid actors is significantly improved. Compared to the OmniRe (Chen et al. 2025) that additionally incorporates SMPL (Loper et al. 2015), our method achieves comparable reconstruction performance (Table 6).

Model	PSNR↑	SSIM↑	LPIPS↓
OmniRe (Chen et al. 2025)	37.26	0.971	0.032
Ours (w/o dynamic)	23.86	0.876	0.110
Ours (w/o deform.)	35.26	0.966	0.036
Ours (full) *	37.93	0.971	0.029

Table 6: Quantitative ablation study results of dynamic optimization module. Dynamic denotes dynamic actors representation module and "deform." denotes the deformable module.

Conclusion

We have introduced the DriveSplat, a novel approach for 3D reconstruction in driving scenarios that enhances the accuracy of both static and dynamic elements. By integrating a partitioned background optimization module with depth and normal priors, our method captures detailed scene geometry for a large-scale background. By tracking the poses of moving vehicles and applying deformable Gaussians to non-rigid actors, dynamic elements achieve a more accurate reconstruction. DriveSplat achieves state-of-the-art performance in novel-view synthesis tasks on two autonomous driving datasets, allowing high-quality geometry representation and large-scale scene reconstruction.

References

Barron, J. T.; Mildenhall, B.; Tancik, M.; Hedman, P.; Martin-Brualla, R.; and Srinivasan, P. P. 2021. Mip-nerf: A multiscale representation for anti-aliasing neural radiance fields. In *Proceedings of the IEEE/CVF International Conference on Computer Vision*, 5855–5864.

Bhat, S. F.; Birk, R.; Wofk, D.; Wonka, P.; and Müller, M. 2023. Zoedepth: Zero-shot transfer by combining relative and metric depth. *arXiv preprint arXiv:2302.12288*.

Cao, A.; and Johnson, J. 2023. Hexplane: A fast representation for dynamic scenes. In *Proceedings of the IEEE/CVF Conference on Computer Vision and Pattern Recognition*, 130–141.

Chen, Y.; Gu, C.; Jiang, J.; Zhu, X.; and Zhang, L. 2023. Periodic vibration gaussian: Dynamic urban scene reconstruction and real-time rendering. *arXiv preprint arXiv:2311.18561*.

Chen, Z.; Yang, J.; Huang, J.; de Lutio, R.; Esturo, J. M.; Ivanovic, B.; Litany, O.; Gojcic, Z.; Fidler, S.; Pavone, M.; et al. 2025. OmniRe: Omni Urban Scene Reconstruction. In *The Thirteenth International Conference on Learning Representations*.

Cheng, K.; Long, X.; Yang, K.; Yao, Y.; Yin, W.; Ma, Y.; Wang, W.; and Chen, X. 2024. GaussianPro: 3D Gaussian Splatting with Progressive Propagation. In *International Conference on Machine Learning*, 8123–8140.

Eftekhari, A.; Sax, A.; Malik, J.; and Zamir, A. 2021. Omnidata: A scalable pipeline for making multi-task mid-level vision datasets from 3d scans. In *Proceedings of the IEEE/CVF International Conference on Computer Vision*, 10786–10796.

Geiger, A.; Lenz, P.; and Urtasun, R. 2012. Are we ready for autonomous driving? the kitti vision benchmark suite. In *2012 IEEE conference on computer vision and pattern recognition*, 3354–3361.

Guo, X.; Sun, J.; Dai, Y.; Chen, G.; Ye, X.; Tan, X.; Ding, E.; Zhang, Y.; and Wang, J. 2023. Forward flow for novel view synthesis of dynamic scenes. In *Proceedings of the IEEE/CVF International Conference on Computer Vision*, 16022–16033.

Huang, B.; Yu, Z.; Chen, A.; Geiger, A.; and Gao, S. 2024a. 2d gaussian splatting for geometrically accurate radiance fields. In *ACM SIGGRAPH 2024 conference papers*, 1–11.

Huang, N.; Wei, X.; Zheng, W.; An, P.; Lu, M.; Zhan, W.; Tomizuka, M.; Keutzer, K.; and Zhang, S. 2024b. S3Gaussian: Self-Supervised Street Gaussians for Autonomous Driving. *arXiv preprint arXiv:2405.20323*.

Jiang, Y.; Tu, J.; Liu, Y.; Gao, X.; Long, X.; Wang, W.; and Ma, Y. 2023. GaussianShader: 3D Gaussian Splatting with Shading Functions for Reflective Surfaces. *arXiv preprint arXiv:2311.17977*.

Kerbl, B.; Kopanas, G.; Leimkühler, T.; and Drettakis, G. 2023. 3D Gaussian Splatting for Real-Time Radiance Field Rendering. *ACM Transactions on Graphics (TOG)*, 42(4): 1–14.

Kerbl, B.; Meuleman, A.; Kopanas, G.; Wimmer, M.; Lanvin, A.; and Drettakis, G. 2024. A hierarchical 3d gaussian representation for real-time rendering of very large datasets. *ACM Transactions on Graphics (TOG)*, 43(4): 1–15.

Li, H.; Li, J.; Zhang, D.; Wu, C.; Shi, J.; Zhao, C.; Feng, H.; Ding, E.; Wang, J.; and Han, J. 2024. VDG: vision-only dynamic gaussian for driving simulation. *arXiv preprint arXiv:2406.18198*.

Li, Z.; Wang, Q.; Cole, F.; Tucker, R.; and Snavely, N. 2023. Dynibar: Neural dynamic image-based rendering. In *Proceedings of the IEEE/CVF Conference on Computer Vision and Pattern Recognition*, 4273–4284.

Lin, H.; Peng, S.; Xu, Z.; Yan, Y.; Shuai, Q.; Bao, H.; and Zhou, X. 2022. Efficient neural radiance fields for interactive free-viewpoint video. In *SIGGRAPH Asia 2022 Conference Papers*, 1–9.

Lin, J.; Li, Z.; Tang, X.; Liu, J.; Liu, S.; Liu, J.; Lu, Y.; Wu, X.; Xu, S.; Yan, Y.; et al. 2024. Vastgaussian: Vast 3d gaussians for large scene reconstruction. In *Proceedings of the IEEE/CVF Conference on Computer Vision and Pattern Recognition*, 5166–5175.

Liu, T.; Wang, G.; Hu, S.; Shen, L.; Ye, X.; Zang, Y.; Cao, Z.; Li, W.; and Liu, Z. 2025a. MVSGaussian: Fast Generalizable Gaussian Splatting Reconstruction from Multi-View Stereo. In *European Conference on Computer Vision*, 37–53. Springer.

Liu, Y.; Luo, C.; Fan, L.; Wang, N.; Peng, J.; and Zhang, Z. 2025b. Citygaussian: Real-time high-quality large-scale scene rendering with gaussians. In *European Conference on Computer Vision*, 265–282.

Lombardi, S.; Simon, T.; Schwartz, G.; Zollhoefer, M.; Sheikh, Y.; and Saragih, J. 2021. Mixture of volumetric primitives for efficient neural rendering. *ACM Transactions on Graphics (ToG)*, 40(4): 1–13.

Loper, M.; Mahmood, N.; Romero, J.; Pons-Moll, G.; and Black, M. J. 2015. SMPL: a skinned multi-person linear model. *ACM Transactions on Graphics (TOG)*, 34(6): 1–16.

Lu, T.; Yu, M.; Xu, L.; Xiangli, Y.; Wang, L.; Lin, D.; and Dai, B. 2024. Scaffold-gs: Structured 3d gaussians for view-adaptive rendering. In *Proceedings of the IEEE/CVF Conference on Computer Vision and Pattern Recognition*, 20654–20664.

Luiten, J.; Kopanas, G.; Leibe, B.; and Ramanan, D. 2023. Dynamic 3d gaussians: Tracking by persistent dynamic view synthesis. *arXiv preprint arXiv:2308.09713*.

Ma, Z.; Jiang, J.; Chen, Y.; and Zhang, L. 2025. B\ezierGS: Dynamic Urban Scene Reconstruction with B\ezier Curve Gaussian Splatting. *arXiv preprint arXiv:2506.22099*.

Mackiewicz, A.; and Ratajczak, W. 1993. Principal components analysis (PCA). *Computers & Geosciences*, 19(3): 303–342.

Martin-Brualla, R.; Radwan, N.; Sajjadi, M. S.; Barron, J. T.; Dosovitskiy, A.; and Duckworth, D. 2021. Nerf in the wild: Neural radiance fields for unconstrained photo collections. In *Proceedings of the IEEE/CVF Conference on Computer Vision and Pattern Recognition*, 7210–7219.

Mildenhall, B.; Srinivasan, P. P.; Tancik, M.; Barron, J. T.; Ramamoorthi, R.; and Ng, R. 2021. Nerf: Representing scenes as neural radiance fields for view synthesis. *Communications of the ACM*, 65(1): 99–106.

Park, K.; Sinha, U.; Hedman, P.; Barron, J. T.; Bouaziz, S.; Goldman, D. B.; Martin-Brualla, R.; and Seitz, S. M. 2021. Hypernerf: A higher-dimensional representation for topologically varying neural radiance fields. *arXiv preprint arXiv:2106.13228*.

Park, S.; Son, M.; Jang, S.; Ahn, Y. C.; Kim, J.-Y.; and Kang, N. 2023. Temporal Interpolation Is All You Need for Dynamic Neural Radiance Fields. In *Proceedings of the IEEE/CVF Conference on Computer Vision and Pattern Recognition*, 4212–4221.

Peng, C.; Zhang, C.; Wang, Y.; Xu, C.; Xie, Y.; Zheng, W.; Keutzer, K.; Tomizuka, M.; and Zhan, W. 2025. Desir3gs: 4d street gaussians for static-dynamic decomposition and surface reconstruction for urban driving scenes. In *Proceedings of the Computer Vision and Pattern Recognition Conference*, 6782–6791.

Peng, S.; Yan, Y.; Shuai, Q.; Bao, H.; and Zhou, X. 2023. Representing Volumetric Videos as Dynamic MLP Maps. In *Proceedings of the IEEE/CVF Conference on Computer Vision and Pattern Recognition*, 4252–4262.

Pumarola, A.; Corona, E.; Pons-Moll, G.; and Moreno-Noguer, F. 2021. D-nerf: Neural radiance fields for dynamic scenes. In *Proceedings of the IEEE/CVF Conference on Computer Vision and Pattern Recognition*, 10318–10327.

Ren, K.; Jiang, L.; Lu, T.; Yu, M.; Xu, L.; Ni, Z.; and Dai, B. 2025. Octree-GS: Towards Consistent Real-time Rendering with LOD-Structured 3D Gaussians. *IEEE Transactions on Pattern Analysis and Machine Intelligence*.

Roessle, B.; Barron, J. T.; Mildenhall, B.; Srinivasan, P. P.; and Nießner, M. 2022. Dense depth priors for neural radiance fields from sparse input views. In *Proceedings of the IEEE/CVF Conference on Computer Vision and Pattern Recognition*, 12892–12901.

Sun, P.; Kretzschmar, H.; Dotiwalla, X.; Chouard, A.; Patnaik, V.; Tsui, P.; Guo, J.; Zhou, Y.; Chai, Y.; Caine, B.; et al. 2020. Scalability in perception for autonomous driving: Waymo open dataset. In *Proceedings of the IEEE/CVF conference on computer vision and pattern recognition*, 2446–2454.

Sun, S.; Zhao, C.; Sun, Z.; Chen, Y. V.; and Chen, M. 2025. SplatFlow: Self-Supervised Dynamic Gaussian Splatting in Neural Motion Flow Field for Autonomous Driving. In *Proceedings of the Computer Vision and Pattern Recognition Conference*, 27487–27496.

Tancik, M.; Casser, V.; Yan, X.; Pradhan, S.; Mildenhall, B.; Srinivasan, P. P.; Barron, J. T.; and Kretzschmar, H. 2022. Block-nerf: Scalable large scene neural view synthesis. In *Proceedings of the IEEE/CVF Conference on Computer Vision and Pattern Recognition*, 8248–8258.

Turkulainen, M.; Ren, X.; Melekhov, I.; Seiskari, O.; Rahtu, E.; and Kannala, J. 2024. Dn-splat: Depth and normal priors for gaussian splatting and meshing. *arXiv preprint arXiv:2403.17822*.

Wang, G.; Chen, Z.; Loy, C. C.; and Liu, Z. 2023. Sparsen-erf: Distilling depth ranking for few-shot novel view synthesis. *arXiv preprint arXiv:2303.16196*.

Wang, S.; Leroy, V.; Cabon, Y.; Chidlovskii, B.; and Revaud, J. 2024. Dust3r: Geometric 3d vision made easy. In *Proceedings of the IEEE/CVF Conference on Computer Vision and Pattern Recognition*, 20697–20709.

Wei, Y.; Liu, S.; Rao, Y.; Zhao, W.; Lu, J.; and Zhou, J. 2021. Nerfingmvs: Guided optimization of neural radiance fields for indoor multi-view stereo. In *Proceedings of the IEEE/CVF International Conference on Computer Vision*, 5610–5619.

Wu, G.; Yi, T.; Fang, J.; Xie, L.; Zhang, X.; Wei, W.; Liu, W.; Tian, Q.; and Wang, X. 2024. 4d gaussian splatting for real-time dynamic scene rendering. In *Proceedings of the IEEE/CVF conference on computer vision and pattern recognition*, 20310–20320.

Xu, J.; Deng, K.; Fan, Z.; Wang, S.; Xie, J.; and Yang, J. 2025. AD-GS: Object-Aware B-Spline Gaussian Splatting for Self-Supervised Autonomous Driving. *arXiv preprint arXiv:2507.12137*.

Yan, Y.; Lin, H.; Zhou, C.; Wang, W.; Sun, H.; Zhan, K.; Lang, X.; Zhou, X.; and Peng, S. 2024. Street gaussians for modeling dynamic urban scenes. *arXiv preprint arXiv:2401.01339*.

Yang, L.; Kang, B.; Huang, Z.; Zhao, Z.; Xu, X.; Feng, J.; and Zhao, H. 2024a. Depth anything v2. *Advances in Neural Information Processing Systems*, 37: 21875–21911.

Yang, Z.; Chen, Y.; Wang, J.; Manivasagam, S.; Ma, W.-C.; Yang, A. J.; and Urtasun, R. 2023. UniSim: A Neural Closed-Loop Sensor Simulator. In *Proceedings of the IEEE/CVF Conference on Computer Vision and Pattern Recognition*, 1389–1399.

Yang, Z.; Gao, X.; Zhou, W.; Jiao, S.; Zhang, Y.; and Jin, X. 2024b. Deformable 3d gaussians for high-fidelity monocular dynamic scene reconstruction. In *Proceedings of the IEEE/CVF conference on computer vision and pattern recognition*, 20331–20341.

Yu, Z.; Chen, A.; Huang, B.; Sattler, T.; and Geiger, A. 2024. Mip-splatting: Alias-free 3d gaussian splatting. In *Proceedings of the IEEE/CVF Conference on Computer Vision and Pattern Recognition*, 19447–19456.

Zhang, D.; Wang, C.; Wang, W.; Li, P.; Qin, M.; and Wang, H. 2024. Gaussian in the wild: 3d gaussian splatting for unconstrained image collections. In *European Conference on Computer Vision*, 341–359. Springer.

Zhou, X.; Lin, Z.; Shan, X.; Wang, Y.; Sun, D.; and Yang, M.-H. 2024. Drivinggaussian: Composite gaussian splatting for surrounding dynamic autonomous driving scenes. In *Proceedings of the IEEE/CVF Conference on Computer Vision and Pattern Recognition*, 21634–21643.

Zhu, Z.; Fan, Z.; Jiang, Y.; and Wang, Z. 2023. FSGS: Real-Time Few-shot View Synthesis using Gaussian Splatting. *arXiv preprint arXiv:2312.00451*.